JOURNAL OF AIRCRAFT
Vol. 47, No. 3, May–June 2010

Exploring the Stability Landscape of Constant-Stress Pumpkin Balloon Designs

Frank Baginski*
George Washington University, Washington, D.C. 20052
and
Kenneth Brakke†
Susquehanna University, Selinsgrove, Pennsylvania 17870

DOI: 10.2514/1.45497

Pumpkin balloon designs such as the constant-bulge-angle design, the constant-bulge-radius design, and hybrids of the constant-bulge-angle and constant-bulge-radius schemes have been used in an attempt to achieve a cyclically symmetric pumpkinlike shape when fully inflated. A number of flight balloons that were built based on the constant-bulge-angle, constant-bulge-radius, and hybrid design strategies encountered deployment problems. In June 2006, Flight 555-NT (a hybrid design) formed an S-cleft and did not deploy. Currently, NASA's approach to superpressure balloon design uses a constant-stress model developed at NASA Goddard Space Flight Center. To fully understand the mechanism behind cleft formation in pumpkin balloons and to explore the constant-stress design space, NASA's Balloon Program Office carried out a series of inflation tests in 2007 involving four 27-meter-diameter 200-gore pumpkin balloons. One of the test vehicles was a one-third-scale mockup of the Flight 555-NT balloon. Using an inflation procedure intended to mimic ascent, the one-third-scale mockup developed an S-cleft feature that was strikingly similar to the one observed in Flight 555-NT. The remaining three 27-meter balloons tested were constant-stress designs and deployed properly. In an effort to gauge constant-stress design susceptibility to deployment problems, we carry out a number of parametric studies and assess the stability landscape of the constant-stress design space. In our studies, we examine two types of top end-fitting boundary conditions, one restrictive and one less restrictive, that help to define a cleft-free design envelope. We correlate our analytical predictions with outcomes of inflation tests involving 27-meter-diameter test vehicles and outcomes from flight 586-NT and flight 591-NT, which involved larger constant-stress designs. To study scaling effects, we consider a 14-million-cubic-foot design. Our analysis suggests that as one scales up the balloon, the size of the cleft-free envelope shrinks.

Nomenclature

BA	=	bulge angle of gore at the equator, deg
D	=	balloon diameter, m
$Df(\boldsymbol{q})$	=	gradient of f with respect to degrees of freedom
f	=	total energy of the balloon system
H	=	balloon height, m
$H_f(\boldsymbol{q})$	=	Hessian matrix (second-order partial derivatives of f), $[\partial^2 f/\partial q_i \partial q_j]$
h	=	balloon film thickness
N	=	number of degrees of freedom in complete shape $\mathcal{S}$
n_g	=	number of gores
p_0	=	nadir pressure
p_1	=	apex pressure
$\boldsymbol{q}$	=	$(q_1, \ldots, q_N)$
$\mathcal{S}$	=	balloon shape
S/C	=	ratio of bulge arc length to tendon-to-tendon chord length at equator
$\|(x, y)\|$	=	$\sqrt{x^2 + y^2}$
$\|(x, y, z)\|$	=	$\sqrt{x^2 + y^2 + z^2}$
λ_{-i}	=	ith negative eigenvalue of H_f, $\lambda_{-i-1} < \lambda_{-i}$
σ_H	=	hoop stress
σ_M	=	meridional stress
$\|\cdot\|$	=	Euclidean norm

Presented as Paper 2814 at the AIAA Balloon Systems Conference, Seattle, WA, 4–7 May 2009; received 17 May 2009; revision received 20 August 2009; accepted for publication 12 October 2009.

*Professor, Department of Mathematics. Senior Member AIAA.
†Professor, Department of Mathematical Sciences.

I. Introduction

FOR large heavy-lift superpressure balloon systems, a pumpkin shape has definite advantages over an axisymmetric shape of comparable size. The lobes in a pumpkin-shaped superpressure balloon allow one to reduce the hoop stress σ_H. Membrane equilibrium implies that $r_B P = h\sigma_H + (r_B/r_M)h\sigma_M$, where h is the thickness of the membrane, r_B is the radius of curvature of the bulge (often called the *bulge radius*), r_M is the other principal radius of curvature, σ_M is the meridional stress, and P is the differential pressure. Since $r_B \ll r_M$, we have that $r_B P \approx h\sigma_H$. Thus, the stress resultant $h\sigma_H$ can be kept at a moderate level by choosing r_B sufficiently small. See Fig. 1 for a schematic of a pumpkin gore. However, as it has been demonstrated in numerous ground tests and balloon flights, choosing r_B too small can lead to deployment problems when a sufficiently high number of gores are involved [1].

The pumpkin-shape concept for a thin compliant pressure vessel goes back to Taylor [2] in his work on parachutes. In the 1970s, Smalley [3] applied the idea of a pumpkin shape to balloons. However, due to a lack of appropriate materials at that time, it was not feasible to develop flight balloons based on this principle. In the late 1980s, Nott's [4] *Endeavour* used a pumpkin design in the race for the first balloon circumnavigation of the globe. In the past decade, NASA's Balloon Program Office has been developing a superpressure balloon in its quest for a long-duration balloon system capable of midlatitude flights.

The literature on thin compliant pressure vessels is extensive and the applications vary. For example, a mathematical model similar to the one presented here was used to carry out a stress analysis of a thin nylon spherical vessel that contained the scintillator for the solar neutrino experiment Borexino [5]. Although the scintillator was shielded by a thick barrier of buffer fluid (of similar density as the scintillator) and the temperature was regulated, experimenters were concerned that in the event of a power failure a sufficient temperature difference between inside and outside fluids would lead to a buoyant

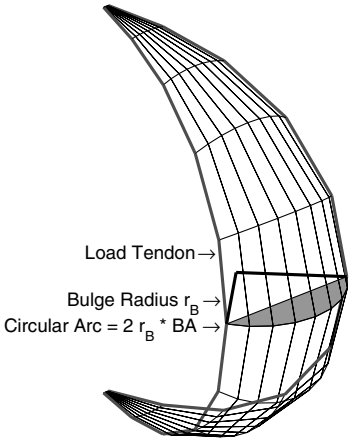

Fig. 1 Schematic of a single pumpkin lobe with tendons. Transverse to each longitude is a circular arc of length $2 \cdot BA \cdot r_B$, where the circle's bulge radius and bulge angle are denoted, r_B and $2 \cdot BA$, respectively. In a constant-bulge-radius design, r_B is constant along the length of the lobe and BA varies. In a constant-bulge-angle design, r_B varies along the length of the lobe and BA is constant. The constant-bulge-angle design has proven to be problematic in regard to deployment [9,13].

scintillator. If the temperature gradient was sufficiently large, a sufficiently high lifting force could be generated, thus damaging the nylon shell or the supporting structure. Another application involves tethered aerostats. Conventional aerostats cannot consistently survive high winds and so the authors of [6] used finite element analysis to assess the performance of tethered vehicles over long periods of time to determine stress concentrations and critical stresses in the envelopes. While the pumpkin balloon problem shares some features with these types of pressure structures, other factors, like the thinness of the balloon envelope, low film stresses, membrane response to internal and external forces, and wrinkling, interact in a way that makes the problem very unique. One of the consequences of wrinkling is shape indeterminacy, i.e., there may be many deformation gradients giving rise to the same membrane stress distribution. Since the lobes in a pumpkin balloon are not molded, but formed from flat panels of thin film, there will be wrinkling at low-to-moderate inflation pressures. One way to avoid the complications due to wrinkling is to consider high-pressure loading scenarios in which wrinkles disappear, the geometry of the deformed shape is well-defined and standard finite element methods can be applied [7]. A severe enabling assumption such as this limits the applicability of subsequent results to important scenarios, including ascent and deployment. We have implemented an efficient computation of Pipkin's energy relaxation approach [8] to wrinkling into our numerical model for the film so that we can study low-, moderate- and high-pressure loading conditions.

We use a two-pronged approach to analyze a family of balloon shapes. First, we carry out an analysis of the desired fully deployed symmetric state and assess the stability landscape of the design space (the primary focus of this paper). Second, we numerically compute alternate asymmetric equilibrium configurations when our stability studies indicate the symmetric shape is not stable. Based on the results of the analysis, we can provide guidance to the balloon designer regarding the likelihood of deployment and what the fully deployed shape might be.

While the schemes behind early pumpkin designs were different, all were susceptible to deployment problems that typically manifested in the form of a cleft. Past experience suggests that the pumpkin balloon is sensitive to small changes in certain design parameters. However, the advantages offered by the pumpkin balloon compel one to investigate the existence of a cleft-free design envelope. Such a region would enable the balloon designer to vary parameters for a particular balloon design and remain confident that the design variations would not lead to an unstable design. The successful deployment of moderately sized 200-gore constant-stress (CS) pumpkin balloons [$(D, H) = (27\text{ m}, 16\text{ m})$ in a controlled test environment and the successful deployments of larger systems with 200 gores, flight 586-NT $(D, H) = (54\text{ m}, 33\text{ m})$ and flight 591-NT $(D, H) = (82\text{ m}, 52\text{ m})$] suggest that a cleft-free envelope is plausible. However, the sensitivity of the pumpkin design and the paucity of available flight data for any one family of designs means that it will be no simple task to determine the cleft-free envelope. In this paper, we will explore the stability landscape of a family of CS designs related to the test vehicles used in 2007. To discuss scaling issues, we consider a 230-gore 14-million-cubic-foot (mcf) design. Previous stability analysis by the authors [9–12] and the 2007 test results suggest that the existence of multiple unstable eigenmodes are a consisent indicator of deployment problems.

In a constant-bulge-angle (CBA) design like *Endeavour*, the radius of the tube that generates the lobe spanning adjacent tendons varies along the gore length while the angular width is kept constant [9]. Nott [4] was one of the first to encounter deployment difficulties with a pumpkin balloon (see Fig. 2a). He and his colleagues surmised correctly that excess material was at the root of *Endeavour*'s deployment problem. Upon removing four gores from the original 64-gore design, they found that the 60-gore balloon deployed ([9], Figs. 1 and 2). How the balloon would have held up over a long flight is open to debate, but suffice it to say that the 60-gore balloon was flown by Nott [4], although at a reduced capacity. Calledine [13] used stability to explain *Endeavour*'s behavior. Using a semi-empirical approach, Calledine argued that he could ignore variations in the strain energy and approximate the principle of minimum potential energy by a maximum volume rule. Calledine found the 60-gore balloon was stable, while the 64-gore balloon was unstable. We carried out a stability analysis that included strain energy of tendons and film and obtained similar results, justifying Calledine's simplfying assumptions in the *Endeavour* analysis (see [9], Fig. 6). These simplifying assumptions would be invalid in the case of large strains [9]. Nevertheless, Calledine's pioneering work highlighted the sensitivity of the pumpkin design to the number of gores and the amount of excess material in a pumpkin lobe.

Some of the early NASA superpressure pumpkin balloons were constant-bulge-radius (CBR) designs. In this scheme, the lobe can be modeled as a subset of a tubular surface with constant-bulge-radius r_B. Although the radius of the tube is constant, the angular width of

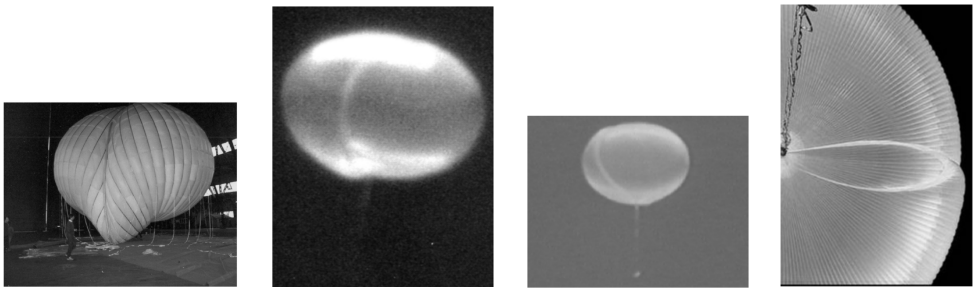

a) Endeavour **b) Flight 496-NT** **c) Flight 517-NT** **d) Flight 555-NT**

Fig. 2 Photographs of balloons with S-clefts.

the tube varies, achieving a minimum near the end fittings and a maximum at the equator. To ensure that the pressurized shape would achieve the intended configuration, the early NASA CBR designs included a fabrication technique called tendon foreshortening. Using the CBR approach, a number of NASA pumpkin designs encountered deployment difficulties. For example, flight 496-NT in 2001 and flight 517-NT in 2003 were unable to deploy properly, locking into a configuration that has come to be known as an S-cleft (see Figs. 2b and 2c). A stability analysis of the flight 517-NT design demonstrated that a combination of excessive tendon foreshortening, excess material, and a large number of gores (290) yielded an unstable design that ultimately led to a balloon that was unable to deploy during a normal ascent [10].

Using empirically derived mechanical properties of the film and tendons in the design process of a large balloon for the first time and incorporating concepts related to the CBA and CBR approaches, a novel hybrid design was used in Flight 555-NT (Sweden, 2006). Even though the lobe in 555-NT $(\mathsf{BA}, \mathsf{S/C}) = (98^\circ, 1.11)$ was not as pronounced as in 517-NT $(\mathsf{BA}, \mathsf{S/C}) = (112^\circ, 1.17)$, the hybrid design was unable to deploy and the S-cleft was observed once again (see Fig. 2d). It is important to point out that not all CBR designs experienced deployment problems. Flight 474-NT successfully deployed on 23 October 1999 and flight 485-NT on 4 June 2000 [11]. However, the CS design incorporates features that favor deployment by keeping excess gore width to a minimum. Because the CS design is the focus of NASA's research and development efforts for a long-duration heavy-lift platform, we restrict our attention to CS designs in this work.

To better understand the S-cleft and what makes a design vulnerable to cleft formation, a series of inflation tests were carried out on a set of four test vehicles at the TCOM Manufacturing and Flight Test Facility in Elizabeth City, North Carolina, in 2007. A goal of this paper is to correlate findings from the 2007 TCOM inflation tests with analytical predictions regarding the susceptibility of the CS design to clefting. Our analytical approach uses stability to assess the design space of a family of CS designs, providing rationale for identifying a cleft-free envelope. Designs that fall in this region would be deemed likely to deploy. While it is impossible to carry out ground testing at the proper scale for large flight-size balloons, we can validate predictions of our mathematical model using ground tests, and then have confidence in our results when the same methods are applied to flight-size balloons. This is important because our work shows that the cleft-free envelope shrinks as the size of the balloon increases.

We begin with an analysis of four test vehicles whose characteristics are summarized in Table 1. BA98H was approximately a one-third-scale mockup of the Flight 555-NT design. BA90CS, BA55CS, and BA27CS were generated by Planetary Balloon, a balloon design code that incorporates the *constant-stress* approach of its author Farley [14]. Designs based on Planetary Balloon will be called constant-stress, or CS, designs. Unlike previous pumpkin designs, a CS design uses empirically derived mechanical properties of the film and tendon to estimate the strained gore shape and tendon configuration, backing out the gore cutting pattern that is needed to achieve the desired strained shape at full inflation.

Consider a balloon design with parameters defined in Table 2. With the hoop stress set to $\sigma_H = 1.73$ MPa, Planetary Balloon calculates that the bulge angle at the equator should be 55.3° and the ratio of the bulge arc length to the tendon-to-tendon chord length is $\mathsf{S/C} = 1.0398$. We will refer to this particular design as BA55CS. A second 27-m-diam balloon (BA90CS) with $\sigma_H = 2.00$ MPa, $p_1 = 86$ Pa, and equatorial bulge angle of 89.8° was also fabricated (see the second column in Table 2). A third balloon (BA27CS) with a bulge angle of roughly 27° was also fabricated. We estimated that $\sigma_H = 3.35$ MPa for BA27CS.

Table 2 Design parameters for BA55CS with $\sigma_H = 1.73$ MPa and BA90CS with $\sigma_H = 2.00$ MPa

	Value	
Parameter	BA55CS	BA90CS
Hoop Stress, σ_H, MPa	1.73	2.00
Tendon stiffness, N	85,000	
Slack strain	0.003	
Density of seal/tendon, kg/m	0.004	
Shell thickness, μm	12.1	
Shell density, kg/m^3	920	
Young's modulus E_1, MPa	152.5	158
Young's modulus E_2, MPa	166.5	162
Poisson's ratio ν_1	0.65	0.60
Poisson's ratio ν_2	0.75	0.70
Apex fitting, kg	2	
Nadir fitting, kg	5	
Apex pressure, p_1, Pa	50	86
Buoyancy, N/m^3	0.1419	0.14123
Film temp, K	302	300

When BA98H was inflated, the balloon assumed a shape (see Figs. 3a and 3b) that was remarkably similar to the cleft observed in Flight 555-NT (see Fig. 2d). BA90CS, BA55CS, and BA27CS properly deployed at a moderately low pressure (see Figs. 4a–4c). After the design pressure was reached in each of the tests, BA90CS, BA55CS, and BA27CS fully deployed and assumed the desired pumpkin shape (see Figs. 4d–4f).

Before we correlate these test results with analysis, we provide a brief summary of our mathematical model, beginning with a description of the end-fitting boundary conditions.

II. End-Fitting Boundary Conditions

We assume that a balloon is situated so that the center of the bottom end fitting is located at the origin of a Cartesian coordinate system. The bottom end fitting is fixed. We consider two types of boundary conditions for the top end fitting. For boundary condition A (BC-A), nodes along the perimeter of the top end fitting are free to move vertically on a cylinder of fixed radius. For boundary condition B (BC-B), the top end-fitting nodes are fixed. Roughly speaking, BC-A is less restrictive than BC-B and one might argue it is not realistic to assume that the end-fitting nodes move unconstrained vertically. However, BC-A does give a indication of how excess material in a strained shape would prefer to distribute itself if it were not restricted by the top end fitting, alerting the balloon designer of possible deployment issues. Conversely, BC-B may be too stringent, but it is difficult to model precisely the interface between the balloon shell/caps/reinforcing tendons and the end fittings. However, using BC-A and BC-B, we are able to make a better assessment of a particular design's likelihood of deployment.

We will demonstrate that a large number of BC-A unstable modes is a consistent indicator of deployment problems, especially if there is still a number of negative eigenvalues when BC-B is applied. We recognize that it is possible for a balloon constrained by BC-B to

Table 1 27-m-diam 200-gore vehicles tested at TCOM in 2007 with boundary conditions BC-A (free top) and BC-B (fixed top) and apex pressure p_1

				Characteristics		
Test vehicle	Fully deployed	BC-A $\lambda_{-i} < 0$	BC-B $\lambda_{-i} < 0$	p_1, Pa	BA, deg	S/C
BA98H	No	7	5	240	98.1°	1.1101
BA90CS	Yes	4	1	86	89.8°	1.1102
BA55CS	Yes	2	0	50	55.3°	1.0398
BA27CS	Yes	0	0	50	26.8°	1.0098

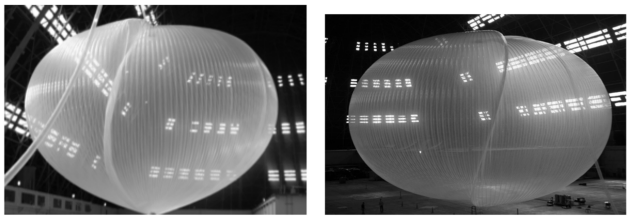

a) 555-NT mockup at $p_0 > 0$ b) 555-NT mockup at $p'_0 > p_0$

Fig. 3 One-third-scale mockup of Flight 555-NT.

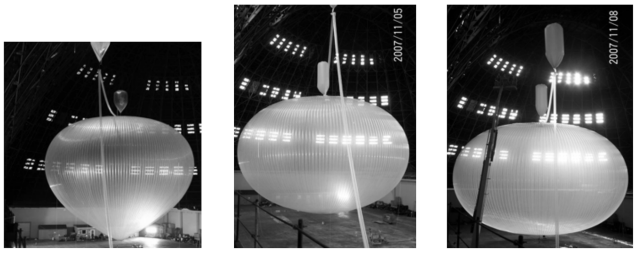

a) BA27CS, deployed b) BA55CS, deployed c) BA90CS, deployed

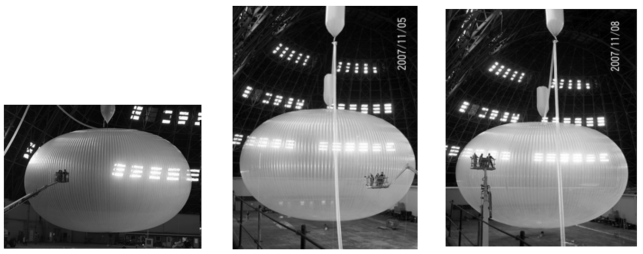

d) BA27CS, at p_0 e) BA55CS, at p_0 f) BA90CS, at p_0

Fig. 4 Photographs of 27-m-diam CS pumpkins at deployment.

possess an unstable mode yet deploy in a normal ascent scenario. For example, BA90CS has four unstable modes under BC-A and one unstable mode under BC-B, yet it fully deployed during an inflation test (see Figs. 4c and 4f). A conservative evaluation of the stability landscape (see Sec. VI) suggests that the BA90CS design is near the boundary of the cleft-free envelope. To the naked eye, some of the alternate asymmetric balloon configurations would be difficult to distinguish from the symmetric equilibrium (see Table 3). To obtain the results in Table 3, let (x, y, z) denote a typical node in the asymmetric equilibrium and (x^0, y^0, z^0) the corresponding node in the symmetric equilibrium; $\max \|(x - x^0, y - y^0, z - z^0)\|$ denotes the maximum displacement from the symmetric equilibrium; $\max \|(x - x^0, y - y^0)\|$ denotes the maximum radial displacement from the symmetric equilibrium.

III. Mathematical Model

In this section, we outline the problem of determining the equilibrium shape of a strained balloon. More details on the model can be found in other references [9,15]. For a complete balloon $\mathcal{S} \subset \mathbb{R}^3$, the reference configuration is $\Omega = \cup_{i=1}^{n_g} G_i$, where G_i is isometric to G_F and G_F is the cutting pattern that is provided by the balloon designer [14]. In this case, $\mathcal{S} = \cup_{i=1}^{n_g} \mathcal{S}_i$, where $\mathcal{S}_i$ is a deformation of G_i. If we restrict our attention to cyclically symmetric shapes, then an equilibrium configuration of a fundamental gore is denoted by $\mathcal{S}_F$. We will describe our model as it applies to a complete balloon.

The total potential energy f of a strained balloon $\mathcal{S}$ is

$$f = \mathcal{E}_P + \mathcal{E}_{\text{film}} + \mathcal{E}_t + \mathcal{E}_{\text{top}} + S_t^* + S_{\text{film}}^* \tag{1}$$

where

$$\mathcal{E}_P = \int_V P(z)\,\mathrm{d}V = -\int_{\mathcal{S}} \left(\frac{1}{2} b z^2 + p_0 z\right) \mathbf{k} \cdot \mathbf{n}\,\mathrm{d}\sigma \tag{2}$$

$$\mathcal{E}_{\text{film}} = \int_{\mathcal{S}} w_{\text{film}} z\,\mathrm{d}A \tag{3}$$

$$\mathcal{E}_t = \sum_{i=1}^{n_g} \int_0^{L_t} \boldsymbol{\alpha}_i(S) \cdot \mathbf{k}\, w_t\,\mathrm{d}S \tag{4}$$

$$\mathcal{E}_{\text{top}} = w_{\text{top}} z_{\text{top}} \tag{5}$$

$$S_t^* = \sum_{i=1}^{n_g} \int_0^{L_t} W_t^*(\epsilon_i)\,\mathrm{d}S \tag{6}$$

$$S_{\text{film}}^* = \int_\Omega W_{\text{film}}^*\,\mathrm{d}A \tag{7}$$

$\mathrm{d}A$ is area measure in the lay-flat reference configuration, $\mathrm{d}S$ is arc length as measured along a tendon in its reference configuration, $\mathcal{E}_P$ is the hydrostatic pressure potential due to the lifting gas, $\mathcal{E}_{\text{film}}$ is the gravitational potential energy of the film, $\mathcal{E}_t$ is the gravitational potential energy of the load tendons, $\mathcal{E}_{\text{top}}$ is the gravitational potential energy of the apex fitting, S_t^* is the total tendon strain energy, and S_{film}^* is the total film strain energy. For the purpose of the analytical studies in this paper, we assume the differential pressure is in the form $-P(z) = bz + p_0$, where p_0 is the known pressure. $V \subset \mathbb{R}^3$ is the region enclosed by $\mathcal{S}$ and $\mathrm{d}V$ is volume measure in $\mathbb{R}^3$. We follow the convention that $-P(z) > 0$ means that the internal pressure is greater than the external pressure; p_0 is the differential pressure at the base of the balloon, where $z = 0$, b is the specific buoyancy of the lifting gas, p_1 is the differential pressure at the apex fitting, $\mathbf{n}$ is the outward unit normal, $\mathrm{d}\sigma$ is surface area measure in the strained balloon surface, w_f is the film weight per unit area, w_t is the tendon weight per unit length, $\boldsymbol{\alpha}_i \in \mathbb{R}^3$ is a parametrization of a deformed tendon with reference configuration Γ_i, w_{top} is the weight of the apex fitting, and z_{top} is the height of w_{top}. The strain in the ith tendon is ϵ_i. $W_t^*(\epsilon_i)$ is the relaxed strain-energy density in the ith tendon. W_{film}^* is the relaxed film strain-energy density. Relaxation of the film strain-energy density is a way of modeling wrinkling [8] in the balloon film and has been used in the analysis of pumpkin-shaped balloons [9–11]. Caps can be incorporated into the model by modifying w_f and W_{film}^* appropriately.

Table 3 Asymmetric equilibria of BA55CS (BC-A) and BA90CS (BC-B)

	BA55CS BC-A			BA90CS BC-B	
	Symmetric	2-lobe	3-lobe	Symmetric	3-lobe
Eigenvalue	——	−0.00996	−0.00466	——	−0.00399
Energy, J	−171, 184	−171, 198	−171, 185	−163, 508	−163, 509
Max z displacement, m	0	0.8721	0.3083	0	0.2115
Max radial displacement, m	0	0.3121	0.1543	0	0.1793
Max total displacement, m	0	0.8749	0.3083	0	0.2136

To determine a strained equilibrium balloon shape, we solve the following:

$$\min_{\mathcal{S}\in\mathcal{H}} f(\mathcal{S}) \tag{8}$$

where $\mathcal{H}$ denotes the class of feasible balloon shapes. Boundary conditions are built into $\mathcal{H}$. In Eq. (8), the continuum problem of finding an equilibrium configuration of the balloon is cast as an optimization problem. This approach is particularly well-suited for the analysis of compliant structures. Surface Evolver [16] is used to calculate symmetric equilibrium shapes and to carry out the stability analysis. Even though the balloon film is orthotropic (see Table 2), we average the two Young's moduli and the two Poisson's ratios to determine a single Young's modulus and Poisson's ratio, so that in effect, the balloon shell is treated as if it were isotropic. Given the comparatively small differences between the E_i and the ν_i, this is a reasonable assumption to make for the types of investigations in this paper.

IV. Stability of Specific CS designs

The degrees of freedom (DOF) in a complete faceted balloon shape $\mathcal{S}$ are the x, y, z coordinates of the nodes of triangular facets $\mathcal{T} \in \mathcal{S}$ that are free to move. Let $\boldsymbol{q} = (q_1, q_2, \ldots, q_N)$ be a list of the DOF. Let $f(\boldsymbol{q})$ be the total energy of a faceted balloon configuration $\mathcal{S} = \mathcal{S}(\boldsymbol{q})$. $Df(\boldsymbol{q}) = [\partial f/\partial q_j]$, $j = 1, \ldots, N$ is the gradient of f evaluated at $\boldsymbol{q}$, where $\partial f/\partial q_j$ denotes partial differentiation with respect to q_j. The Hessian of f evaluated at $\boldsymbol{q}$ is the $N \times N$ matrix, $H_f(\boldsymbol{q}) = D^2 f(\boldsymbol{q}) = [\partial^2 f/\partial q_i \partial q_j]$, $i, j = 1, \ldots, N$. Note that $f(\boldsymbol{q})$, $Df(\boldsymbol{q})$, and $H_f(\boldsymbol{q})$ are computed exactly for the discretization $\mathcal{S}(\boldsymbol{q})$. We are led to the following definition of stability.

Definition: Let $\mathcal{S} = \mathcal{S}(\boldsymbol{q})$ be a solution of Eq. (8). We say $\mathcal{S}$ is *stable* if all the eigenvalues of $H_f(\boldsymbol{q})$ are positive. We say $\mathcal{S}$ is *unstable* if at least one eigenvalue of $H_f(\boldsymbol{q})$ is negative. We say that the stability of $\mathcal{S}$ is *indeterminate* if the lowest eigenvalue of $H_f(\boldsymbol{q})$ is zero.

In theory, the fully inflated shape should be cyclically symmetric so that the loads are distributed uniformly over the entire balloon. If we assume a priori that the strained balloon shape is cyclically symmetric, Eq. (8) can be solved for a half-gore and $\mathcal{S}_F$ can be determined. $\mathcal{S}_F$ is indeed a stable local equilibrium within the class of cyclically symmetric shapes. However, within the larger class of feasible *complete* balloon shapes $\mathcal{H}$, the complete balloon generated by $\mathcal{S}_F$ could turn out to be unstable [11].

A. Boundary Condition A (BC-A)

When the top end-fitting nodes are free to move vertically, we find that BA98H ($p_1 = 240$ MPa) has seven unstable modes. The lowest eigenvalue of BA98H is denoted by λ_{-7} and corresponds to a five-lobe symmetry. The remaining negative eigenvalues ordered from most negative to least negative correspond to six-lobe, four-lobe, seven-lobe, three-lobe, eight-lobe, and two-lobe symmetry, respectively. In the first line of Table 4, we present the unstable modes for BC-A, i.e., those modes that correspond to negative eigenvalues of H_f. By convention, $\lambda_{-i-1} < \lambda_{-i}$.

Applying BC-A, we found that BA90CS ($p_1 = 86$ MPa) had four unstable modes, BA55CS ($p_1 = 50$ MPa) had two unstable modes and BA27CS had no unstable modes. In Figs. 5a and 5b, we present two-lobe and three-lobe equilibria that were evolved based on the two negative eigenvalue modes that were found when applying BC-A to BA55CS. Physical characteristics of these balloons along with the maximal displacements from the symmetric shape are presented in Table 3. We say that a shape has k-lobe symmetry if it is composed of k symmetric components.

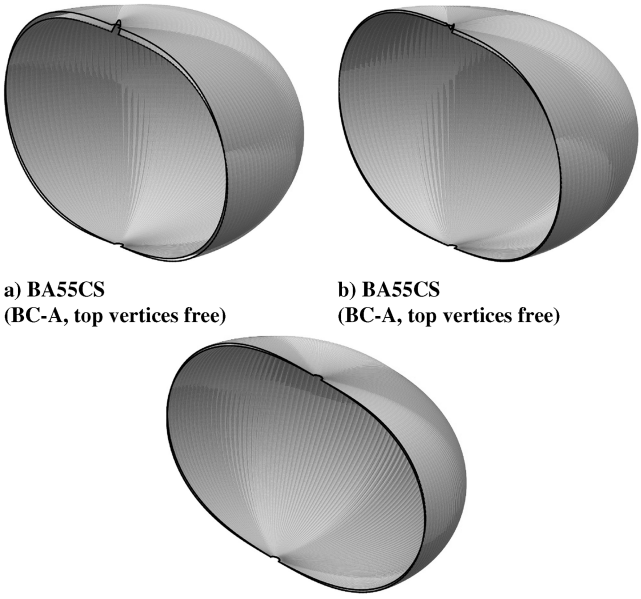

a) BA55CS (BC-A, top vertices free)

b) BA55CS (BC-A, top vertices free)

c) BA90CS (BC-B, top vertices fixed)

Fig. 5 Asymmetric equilibria of CS designs. Each image is the superpositions of a symmetric equilibrium shape (shaded dark) and a lobed equilibrium shape (shaded light).

B. Boundary Condition B (BC-B)

BA98H had five negative eigenvalues with the top end fitting fixed. When these eigenvalues are ordered from most negative to least negative, they correspond to eigenmodes with five-lobe, six-lobe, four-lobe, seven-lobe, and three-lobe symmetry, respectively. The ordering is the same as the first five negative eigenvalues when BC-A is applied (see the second line in Table 4). With the top end fitting fixed, BA55CS and BA27CS had no negative eigenvalues, while BA90CS had one negative eigenvalue $\lambda_{-1} = -0.00399$ with a three-lobe eigenmode (see Table 3). An evolved equilibrium with top end fitting fixed (BC-B) and three-lobe symmetry is displayed in Fig. 5c.

Because a slightly different gore pattern was used in [12] (Table 2, case $\delta = 0$), the results there are slightly different.

V. Cutting Patterns

The cutting pattern in a pumpkin balloon is sensitive to small perturbations in the parameters that define it. While one cutting pattern might give rise to a stable design, a second very similar pattern could lead to an unstable design. For this reason, we need to quantify the differences between such designs. As a benchmark for comparison purposes, we will use the flat-facet pattern from BA55CS that is obtained by spanning two contiguous tendons of the fully inflated symmetric balloon with a developable surface. By

Table 4 BA98H boundary conditions; (BC-A) top end-fitting nodes move vertically and (BC-B) top end-fitting nodes are fixed; negative eigenvalues with symmetry of k lobes

		Eigenvalue (k)-lobe symmetry						
Endcap condition	Unstable modes	λ_{-7}	λ_{-6}	λ_{-5}	λ_{-4}	λ_{-3}	λ_{-2}	λ_{-1}
BC-A	7	−0.4168 (5)	−0.3873 (6)	−0.3791 (4)	−0.2859 (7)	−0.2740 (3)	−0.1232 (8)	−0.1180 (2)
BC-B	5	——	——	−0.2590 (5)	−0.2249 (6)	−0.2157 (4)	−0.1122 (7)	−0.0988 (3)

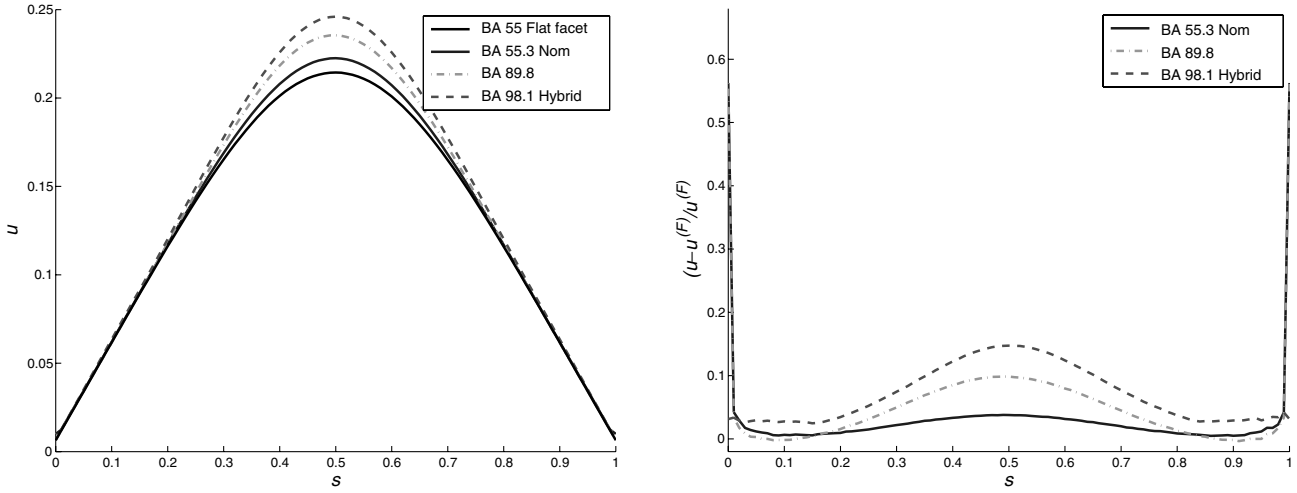

a) Half-gore patterns **b) Cutting patterns and flat facet pattern differences**

Fig. 6 Comparison of cutting patterns for BA55CS, BA90CS, and BA98H; $0 < s < 1$ is normalized gore length.

flattening out this surface, we obtain the pattern labeled BA 55 Flat Facet in Fig. 6a. The flat-facet design is not a viable cutting pattern, it merely gives us a point of reference when comparing other cutting patterns. We then compare this pattern with the cutting patterns for BA55CS, BA90CS, and BA98H. In Fig. 6a, we present these four patterns. We normalized the lengths of each gore to be one ($0 \le s \le 1$), and let $u^{(F)}(s)$, $u^{(90)}(s)$, $u^{(98)}(s)$, and $u^{(55)}(s)$ be the gore half-widths of the BA 55 flat facet, BA90CS, BA98H, and BA55CS, respectively. In Fig. 6b, we plot $(u^{(98)} - u^{(F)})/u^{(F)}$, $(u^{(90)} - u^{(F)})/u^{(F)}$, and $(u^{(55)} - u^{(F)})/u^{(F)}$ as a functions of s. It is clear BA98H is the widest of the patterns, followed by BA90CS, and BA55CS. It is interesting to note that there were two intervals near the end fittings, where BA90CS is a bit narrower than BA55CS. In fact, if we let v denote the gore length ($v = 0$ at the top and $v = 34.6$ m at the bottom), we find that for 2.76 m $< v <$ 3.8 m and 30.45 m $< v <$ 31.83 m, the BA90CS gore pattern is narrower than the flat-facet pattern.

Remark: Since the 2007 inflation tests at TCOM, there have been two successful deployments of flight balloons: flight 586-NT launched from Fort Sumner, New Mexico, in spring 2008 and flight 591-NT, launched from Antarctica in winter 2008. Flight 591-NT set an endurance record by staying aloft more than 54 days. Physical dimensions, characteristics, and design parameters for these designs and a 230-gore 14.836-million-cubic-foot (mcf) design are presented in Table 5.

VI. Stability Landscape

For CBR designs, it was very revealing to carry out stability studies for two parameter families involving the bulge radius and the number of gores [9–12]. While the bulge radius is no longer constant in the CS design, we can vary the hoop stress parameter σ_H in Planetary Balloon and track the bulge radius at the equator. For example, fix the number of gores n_g. Since $r_B P \approx h\sigma_H$, we see that as σ_H decreases, at the equator, the bulge radius r_B must decrease and S/C must increase.

To begin an assessment of the stability landscape of the CS designs, we generated a two parameter family of designs by varying σ_H and n_g. We began with the file that was used to generate the gore pattern for the design BA55CS, where $(n_{g,d}, \sigma_{,d}) =$ (200, 1.73 MPa). In this case, we found the equatorial bulge angle was BA $= 55.3°$ and S/C $= 1.0398$. We then varied n_g over the interval $160 \le n_g \le 260$ and the hoop stress parameter over the interval 0.79 MPa $< \sigma_H <$ 5.50 MPa.

Remark: The minimum value of σ_H depends on n_g. Within the family considered here, our largest equatorial bulge angle was 151.6° and the smallest equatorial bulge angle was 16.6°. In theory, BA can approach a maximum of 180° and a minimum of 0°, but it was not necessary to compute the patterns for these extreme cases.

For each design with (n_g, σ_H), we calculated the corresponding S/C value. In Fig. 7a, each $(n_g, \text{S/C})$ corresponds to a point in

Table 5 Flight-size balloons for flights 586-NT and 591-NT successfully deployed

Parameter	586-NT 2.008 mcf	591-NT 7.093 mcf	14.84 mcf[a]
σ_H, MPa	4	7	10
Diameter, m	54.47	82.541	105.859
Height, m	33.357	51.777	65.913
S/C	1.0397	1.0092	1.0179
Film thickness, μm	38.1	38.1	38.1
Cap thickness, μm	——	——	38
Volume, m^3	56,791	200,691	420,389
Apex pressure, Pa	200	125	185
Nadir pressure, Pa	195.284	120.56	179.377
n_g	200	200	230
BA, deg	55.2	26.8	37.3
r_B, m	0.924	2.8	2.262
Young's moduli	152.5, 166.5	158, 162	137, 164
Poisson's ratios	0.65, 0.75	0.6, 0.7	0.58, 0.692
BC-A ($\lambda_{-i} < 0$)	3	1	2
BC-B ($\lambda_{-i} < 0$)	0	0	0

[a]The 14.84 mcf design has not flown and is presented to illustrate stability issues related to size.

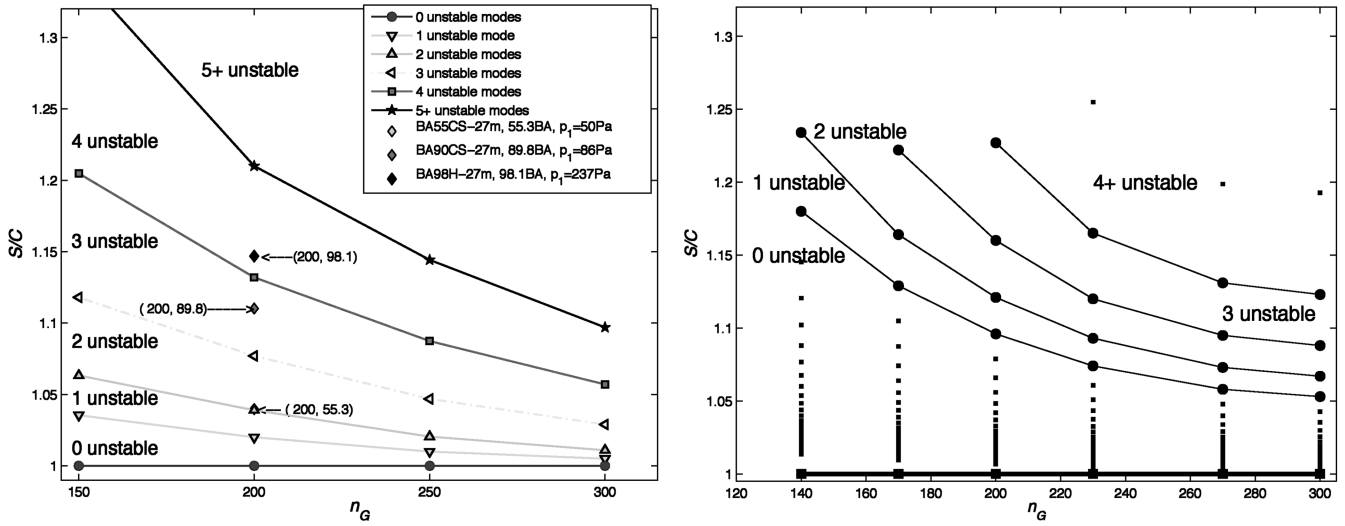

a) Top free b) Top fix

Fig. 7 Stability landscape for a family of 27-m-diam constant-stress designs; (200, 98.1) corresponds to the 27 m 555-NT hybrid, (200, 89.8) corresponds to BA90CS, and (200, 55.3) corresponds to BA55CS. Because $p_1 \neq 50$ Pa, the designs corresponding to (200, 98.1) and (200, 89.8) are not part of the BA55CS family. They are included to demonstrate the design sensitivity.

design space that is classified by the number of unstable modes. The horizontal line in Fig. 7a corresponds to designs with $\mathsf{S/C} = 1$. Above that line is a curve that denotes the boundary between designs with one unstable mode and designs with zero unstable modes. Bandlike regions with no unstable modes, one unstable mode, two unstable modes, three unstable modes, four unstable modes, and five or more unstable modes of BC-A type are identified in Fig. 7a. Next, we consider the same family of balloon designs as analyzed in Fig. 7a, except this time we impose the more restrictive boundary condition BC-B (top endcap fixed). We follow the same scheme in presenting our results. At nadir pressure $p_0 = 50$ Pa, we find the number of top-fixed unstable modes are two for $(n_g, \mathsf{BA}) = (200, 98.0)$, one for $(n_g, \mathsf{BA}) = (200, 89.8)$, and zero for BA55CS $(n_g, \mathsf{BA}) = (200, 55.3)$, respectively. See Fig. 7b for $p_0 = 50$ Pa results related to the BA55CS design family. From Figs. 7a and 7b, one would conclude that the BA98H is unacceptable and BA90CS is borderline unacceptable. BA55CS has two unstable (top-free) BC-A modes. When we compute asymmetric equilibria corresponding to the unstable two-lobe and three-lobe modes, we find that they deviate very little from the symmetric shape. BA55CS falls into the no-unstable-modes region for the top-fixed boundary condition and so BA55CS could be considered a viable design.

Remark: Strictly speaking, since $p_1 = 86$ Pa, BA90CS is not a member of the family presented in Fig. 7a. The same can be said for BA98H, since $p_1 = 240$ in that case. Once a particular design has been selected by the balloon designer, these observations suggest that parametric studies involving the constant pressure term warrant further investigation. Note that many designs in this family may be rejected by the balloon designer, but in this paper we are only looking at stability.

Figure 7 reveals that one must be cautious when applying the stability results to designs with similar $(n_g, \mathsf{S/C})$, but significantly different sizes. For example, flight 586-NT was essentially a scaling of BA55CS by a factor of 2 (an exact scaling of all parameters is not possible to achieve). While BA55CS had two BC-A unstable modes, a stability analysis of the design for flight 586-NT finds three BC-A unstable modes. Similarly, BA27CS had zero BC-A unstable modes, but a stability analysis of flight 591-NT's design indicates one BC-A unstable mode. Neither the 586-NT nor the 591-NT designs had BC-B unstable modes (see Table 5). To further probe this scaling issue, we consider the 230-gore 14.836 mcf design with the characteristics summarized in Table 5. We generated a $(n_g, \mathsf{S/C})$ landscape for the (BC-A) top-free boundary condition (see Fig. 8a) and the BC-B top-fixed boundary condition (see Fig. 8b). The particular design outlined in Table 5 falls into the two unstable top-free modes region and well within the no-unstable-top-fixed-modes region. Because the design apex pressure and balloon size are different in the respective families, one should not expect that the stability landscapes in Figs. 7 and 8 to be the same. This topic merits additional study, especially if, for example, there is a need to fly a larger balloon with 300 gores. For such a design, the unstable-mode regions will more compressed, in the region of interest, where $n_g \approx 300$.

Remark: While BC-A may be an unrealistic condition, it is prudent to be conservative and to apply this criterion when evaluating a design. If a design is stable (or has relatively few unstable modes) under less strict conditions, it is more likely that the real balloon will deploy. For example, a good design is one in which even if we allow vertices along the top end fitting freedom to move vertically, the corresponding asymmetric equilibrium deviates very little from the cyclically symmetric shape. On the other hand, BC-B may be too restrictive, leading one to conclude that the design is stable, when in fact, the stability is due in part to the restrictive boundary condition. By being too restrictive, certain unstable modes might be suppressed. For this reason, we consider both BC-A and BC-B when evaluating a particular design.

VII. Eigenmodes

Our results here and in previous works [9–12] suggest that the S-cleft does not correspond to a single unstable eigenmode: rather, it is deployment-path-dependent. If a large number of alternative configurations are available (as indicated by the large number of unstable modes that are near the fully symmetric state), it stands to reason that a dynamical system like an ascending pumpkin balloon will not fall into the fully symmetric state.

It is a natural question to ask what are the modes that correspond to the seven negative eigenvalues for BA98H or the other CS designs. Using Surface Evolver, the second author generated eigenvectors corresponding to the seven negative eigenvalues of BA98H. These are displayed in Fig. 9. An asymmetric two-lobe equilibrium was calculated in a previous paper by the authors (see [12], Figs. 4a and 4b). While the mode is somewhat unrealistic (displacements of the top end-fitting nodes can vary nearly 0.5 m about the mean), it does indicate there is excess material in the upper region of the balloon, which may make the balloon vulnerable to the S-cleft. BA98H had about 10 gores that were involved in the formation of the S-cleft (the remaining gores appeared to be fully deployed). During the inflation test, it was possible to move the S-cleft from one contiguous collection of gores to another contiguous collection of gores of the

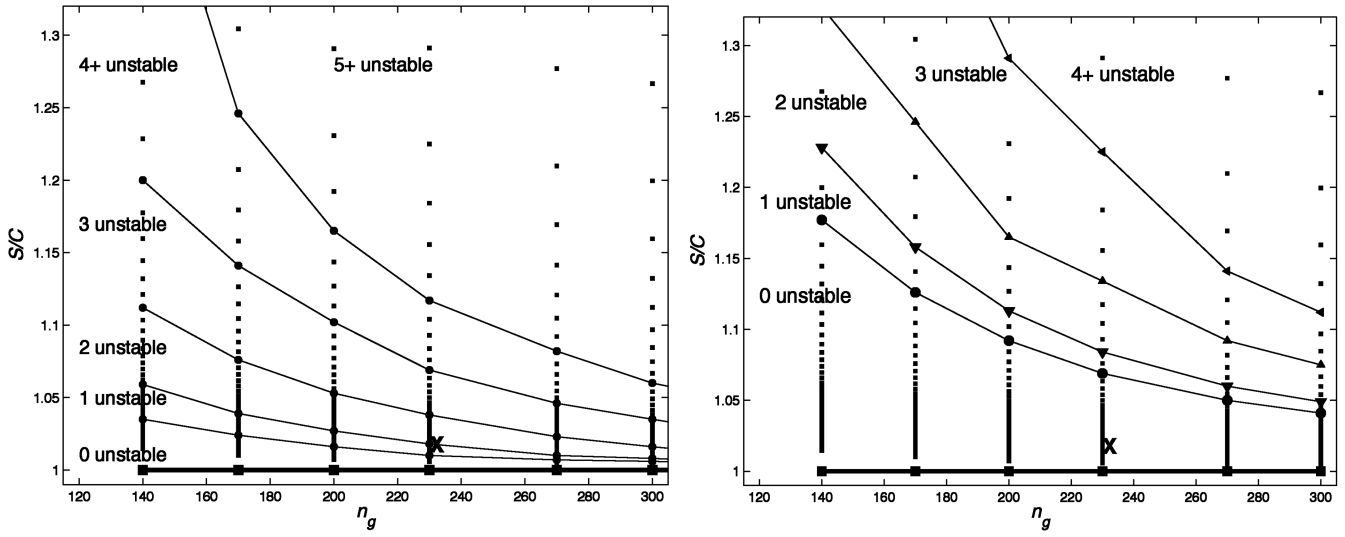

a) BC-A: top free

b) BC-B: top fixed

Fig. 8 Stability landscape for 230-gore 14.8 mcf constant-stress designs; (n_g, S/C) family.

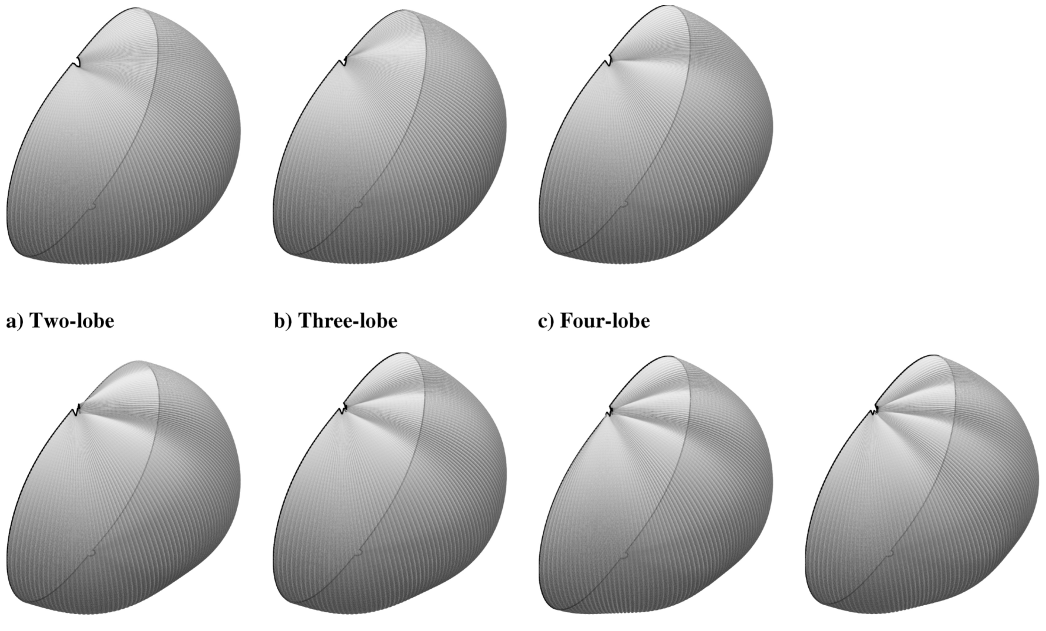

a) Two-lobe b) Three-lobe c) Four-lobe

d) Five-lobe e) Six-lobe f) Seven-lobe g) Eight-lobe

Fig. 9 Unstable modes of one-third-scale mockup of Flight 555-NT design. The displayed eigenmodes are not evolved to equilibrium and their amplitude was chosen to illustrate their respective features.

same number. However, one cannot say with certainty that the S-cleft is the unique shape that BA98H prefers.

VIII. Cleft-Free Envelope in Design Space

Consider the family of CS designs presented in Fig. 7. For the sake of the following discussion, we select the region below the two unstable-mode curve as the cleft-free design envelope. Recall that designs below this line have, at most, one BC-A unstable modes. Note that if we increase p_1 from 50 to 86 Pa, the boundary curves would move downward and the cleft-free envelope would be reduced. In view of the fact that BA98H had seven BC-A unstable modes and five BC-B unstable modes, it is clear that BA98H was a poor design.

Our analysis of the flight-size balloons shows that we cannot look at only the S/C ratio and apply the 27-m-diam results in Fig. 7 to flight balloons like 586-NT and 591-NT. However, once the balloon designer has an estimate of a particular design, it would be expedient to generate a family of designs and carry out a landscape sensitivity study for the corresponding family, as we did for the 14.8 mcf design presented in Fig. 8. Note that the 230-gore 14.836 mcf design has only two BC-A unstable modes and no BC-B unstable modes. These unstable modes corresponded to shapes with two-lobe and three-lobe symmetry. Equilibrium configurations based on these eigenmodes were evolved and they are presented in Fig. 10.

The existence of an unstable mode does not necessarily mean that such a design will not deploy. For example, BA90CS had four BC-A unstable modes and one BC-B unstable mode. During the 2007 test of this vehicle, it clearly deployed (see Fig. 4c and Fig. 4f). However, it is still not clear if the deployed state was the fully symmetric one. To the naked eye, it would be difficult to tell the difference between the three-lobe equilibrium and a symmetric equilibrium. The

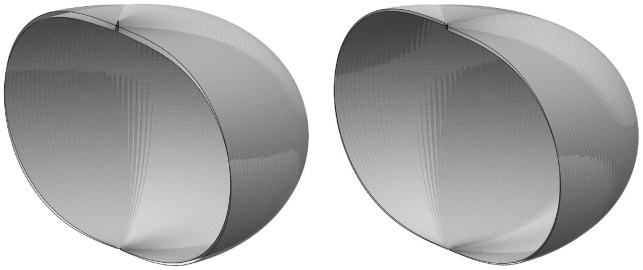

a) b)

Fig. 10 Asymmetric equilibrium configurations of a 230-gore 14.836 mcf balloon: a) two-lobe symmetry and b) three-lobe symmetry with top end-fitting-free condition (BC-A) applied. Each image is the superposition of a symmetric equilibrium shape (shaded dark) and a lobed equilibrium shape (shaded light).

maximum displacement (0.213 m) occurs at about 25 deg from the vertical (see Table 3), so the top would look like the symmetric balloon in that region.

The fact that BA90CS deployed into a shape that is nearly symmetric does not mean that this is a safe design. Based on Fig. 7, there are nearby designs with more unstable modes. Moreover, it is not clear how this balloon would fare over time, due to the fact that the loading is no longer symmetric and the film is viscoelastic.

IX. Conclusions

In this paper, we use stability analysis in an effort to establish guidelines that can assist the balloon designer in assessing the susceptibility of a CS-balloon design to deployment problems. Based on corroborating tests results from 27-m-diam 200-gore CS designs, we conjecture that a large number of unstable modes of the fully symmetric equilibrium shape is an indicator for deployment problems. Flight 586-NT deployed at a much higher altitude and higher pressure than was expected based on the testing done with physical models in 2007. The landscape stability explorations presented here merely scratch the surface of the design space. However, the tools offer some guidance to the design engineer. We have seen that the larger the balloon, the smaller the cleft-free envelope, intimating that extrapolated results from an analysis of small balloon should not be a substitute for a full analysis of the large structure. Nevertheless, because we have validated our mathematical model with test results involving realistic structures, we can be more confident of our analytical predictions applied to large balloons. While the analysis presented here indicates the plausibility of a cleft-free design envelope for deployment assessment, significantly more flight data are needed in order for the balloon design engineer to establish safe operating design margins for large balloons.

Acknowledgments

The first author would like to thank Rodger Farley, NASA Goddard Space Flight Center, for his assistance in the use of Planetary Balloon and for numerous illuminating discussion on the constant-stress balloon design. The authors would like to thank David Pierce, Chief, NASA Balloon Program Office, for the opportunity to collaborate with the Super Pressure Team and for the use of NASA photographs. Thanks to Julian Nott for the use of the *Endeavour* photograph.

References

[1] Schur, W. W., and Jenkins, C. H., "Deployment Destiny, Stable Equilibria, and the Implications for Gossamer Design," 43nd AIAA/ASME/ASCE/AHS/ASC Structures, Structural Dynamics and Materials Conference and Exhibit, AIAA Paper 2002-1205, Denver, CO, 2002.

[2] Taylor, G. I., "On the Shapes of Parachutes," *The Scientific Papers of G. I. Taylor*, Vol. 3, edited by G. K. Batchelor, Cambridge Univ. Press, Cambridge, England, U.K., 1919, pp. 26–37.

[3] Smalley, J. H., "Development of the e-Balloon," National Center for Atmospheric Research, AFCRL-70-0543, Boulder, CO, June 1970.

[4] Nott, J., "Design Considerations and Practical Results with Long Duration Systems for Manned World Flights," *Advances in Space Research*, Vol. 33, No. 10, 2004, pp. 1667–1673. doi:10.1016/j.asr.2003.07.038

[5] Benziger, J., Cadonati, L., Calaprice, F., de Haas, E., Fernholz, R., Ford, C., et al., "The Nylon Scintillator Containment Vessels for the Borexino Solar Neutrino Experiment," *Nuclear Instruments & Methods in Physics Research, Section A*, Vol. 582, No. 2, 2007, pp. 509–534. doi:10.1016/j.nima.2007.08.176

[6] Miller, J. I., and Nahon, M., "Analysis and Design of Robust Helium Aerostats," *Journal of Aircraft*, Vol. 44, No. 5, 2007, pp. 1447–1458. doi:10.2514/1.25627

[7] Pagitz, M., and Pellegrino, S., "Buckling Pressure of 'Pumpkin' Balloons," *International Journal of Solids and Structures*, Vol. 44, No. 21, 2007, pp. 6963–6986. doi:10.1016/j.ijsolstr.2007.03.021

[8] Pipkin, A. C., "Relaxed Energy Densities for Large Deformations of Membranes," *IMA Journal of Applied Mathematics*, Vol. 52, No. 3, 1994, pp. 297–308. doi:10.1093/imamat/52.3.297

[9] Baginski, F., Brakke, K., and Schur, W., "Unstable Cyclically Symmetric and Stable Asymmetric Pumpkin Balloon Configurations," *Journal of Aircraft*, Vol. 44, No. 3, 2007, pp. 764–772. doi:10.2514/1.20874

[10] Baginski, F., Brakke, K., and Schur, W., "Cleft Formation in Pumpkin Balloons," *Advances in Space Research*, Vol. 37, No. 11, 2006, pp. 2070–2081. doi:10.1016/j.asr.2005.04.104

[11] Baginski, F., Brakke, K., and Schur, W., "Stability of Cyclically Symmetric Strained Pumpkin Balloon Configurations and the Formation of Undesired Equilibria," *Journal of Aircraft*, Vol. 43, No. 5, 2006, pp. 1414–1423. doi:10.2514/1.21514

[12] Baginski, F., and Brakke, K., "Simulating Clefts in Pumpkin Balloons," *Advances in Space Research*, Vol. 45, No. 4, 2010, pp. 473–481. doi:10.1016/j.asr.2009.10.022

[13] Calledine, C. R., "Stability of the Endeavour Balloon," *Buckling of Structures*, edited by I. Elishakoff, J. Arbocz, C. D. Babcock, Jr., and A. Libai, Elsevier, New York, 1988, pp. 133–149.

[14] Farley, R., "Planetary Balloon: Balloon Design Software Manual," NASA Goddard Space Flight Center, Greenbelt, MD, 2007.

[15] Baginski, F., Barg, M., and Collier, W., "Existence Theorems for Tendon Reinforced Thin Wrinkled Membranes Subjected to a Hydrostatic Pressure," *Mathematics and the Mechanics of Solids*, Vol. 13, No. 6, 2008, pp. 532–570. doi:10.1177/1081286507077256

[16] Brakke, K., "The Surface Evolver," *Experimental Mathematics*, Vol. 1, No. 2, 1992, pp. 141–165; also The Surface Evolver, Software Package, Ver. 2.30, Jan. 2008, www.susqu.edu/brakke/evolver [retrieved Jan. 2010].